Article

Large-scale tungsten fibre-reinforced tungsten and its mechanical properties

Daniel Schwalenberg [1,6‡], Jan Willem Coenen [1,2,‡*], Johann Riesch [3,], Till Hoeschen, [3,‡], Yiran Mao [1], Alexander Lau [1], Hanns Gietl [4], Leonard Raumann [1], Philipp Huber [5‡] and Christian Linsmeier[1], Rudolf Neu [2,6]

[1] Forschungszentrum Jülich GmbH, Institut für Energie- und Klimaforschung, 52425 Juelich, Germany;
[2] Department of Engineering Physics, University of Wisconsin - Madison, Madison, WI 53706, USA
[3] Max-Planck-Institut für Plasmaphysik, 85748 Garching, German;
[4] Fusion Safety Program, Idaho National Laboratory,Idaho Falls,ID 83412 USA;
[5] Institut für Textiltechnik (ITA) der RWTH Aachen University, 52074 Aachen, Germany;
[6] Technische Universität München, 85748 Garching, Germany;
* Correspondence: j.w.coenen@fz-juelich.de; Tel.: +49 2461615536
‡ These authors contributed equally to this work.

Abstract: Tungsten fibre-reinforced tungsten composites (W_f/W) have been in development to overcome the inherent brittleness of tungsten as one of the most promising candidate for the first wall and divertor armour material in a future fusion power plant. As the development of W_f/W continues, the fracture toughness of the composite is one of the main design drivers. In this contribution the efforts on size upscaling of W_f/W based on Chemical Vapour Deposition (CVD) is shown together with fracture mechanical tests of two different size samples of W_f/W produced by CVD. Three-point bending tests according to ASTM E399 for brittle materials were used to get a first estimation of the toughness. A provisional fracture toughness value of up to 346 $MPa\,m^{1/2}$ was calculated for the as-fabricated material. As the material does not show a brittle fracture in the as-fabricated state, the J-Integral approach based on the ASTM E1820 was additionally applied for this state. A maximum value of the J-integral of 41 kJ/m^2 (134, 8 $MPa\,m^{1/2}$) was determined for the largest samples. Post mortem investigations were employed to detail the active mechanisms and crack propagation.

Keywords: Composites, Fusion, Materials)

Citation: Lastname, F.; Lastname, F.; Lastname, F. Large-scale tungsten fibre-reinforced tungsten and its mechanical properties. *Preprints* **2022**, *1*, 0. https://doi.org/

1. Introduction

Tungsten (W) components are currently considered as the primary candidate for the first wall and divertor armour of existing and future fusion reactors. Tungsten has a very low sputtering yield, the highest melting point of any metal, and behaves relatively well in terms of its properties after neutron irradiation. With respect to the interaction with the fusion fuel, tungsten shows low retention of hydrogen isotopes including tritium.

Much of the existing work regarding tungsten has focussed on qualification towards ITER [1][1–4] and beyond. For the next steps e.g. a Demonstration Reactor (DEMO),[2] the imposed limits for the use of tungsten will be extremely challenging as much of what is determined as boundary conditions [5,6] materials will be above the technical feasibility limits as they are set out today [3,7].

New concepts for plasma-facing components (PFCs) are being studied (see [2,8], and references therein) concentrating on crack resilient materials with low activation, small or no fuel retention, extended lifetime with respect to low erosion and brittle failure. This is due to the fact that the inherent brittleness below the ductile-to-brittle transition temperature of tungsten (DBTT) [9,10] and the embrittlement during operation, e.g. by overheating [11] and/or neutron irradiation [12,13] are the main drawbacks and limit for its use in terms of lifetime considerations.

In Figure 1 the typical properties necessary for fusion are highlighted. The core blue area being the status quo. In essence it means that in particular the areas of oxidation and

---

[1] https://www.iter.org
[2] https://www.euro-fusion.org/programme/demo/

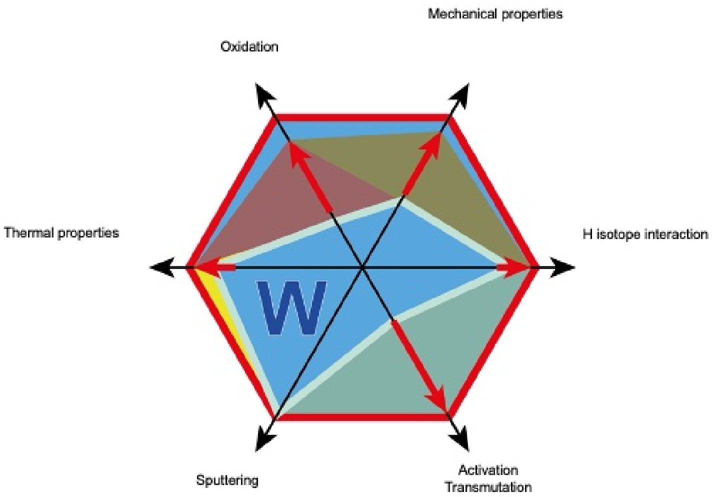

Figure 1. W as first wall and divertor material is still facing challenges. The red lines give the performance with respect to ideal behaviour, represented by the outline of the hexagon. the core blue area is the status quo [8].

mechanical properties need to be improved upon.

In this contribution the efforts on size upscaling of W_f/W based on Chemical Vapour Deposition (CVD) is shown followed by the description of fracture mechanical tests of CVD W_f/W.

2. Tungsten Fibre-Reinforced Tungsten

To overcome the brittleness of W a W composite material (W_f/W), incorporating extrinsic toughening mechanisms as described in [8,14] is being developed. The basic concept of materials such as W_f/W makes use of a composite approach as highlighted in figure 2.

The issue with tungsten essentially is the same as for all brittle materials. Failure occurs in a sudden manner, immediately when the Ultimate Tensile Strength (UTS) is reached. UTS here is statistically distributed and not well defined as it is determined by the weakest point in the material (Weibull statistics). For a materials with well defined material properties, e.g. with high toughness and ductility, the material is intrinsically failure tolerant, with no sudden failure and remains load bearing, beyond UTS, also allowing cyclic loading of the material.

In order to improve brittle materials such as W several options are at hand: microstructural refinement, alloying or composites [15–21]. Regarding W_f/W extrinsic toughening mechanisms are employed thus potentially allowing to overcome material changes due to operational embrittlement by temperature and neutrons.

When considering W_f/W it is important to note that there are various ways of production including CVD [22,23] and powder metallurgical (PM) processes [24–28]. The chemical vapour deposition of tungsten is frequently used for the production of W_f/W as it allows low processing temperatures and a force-free production. The used process is the heterogeneous surface reaction of WF_6 and H_2 to form a solid W deposit and gaseous HF. This process is highly sensitive to the partial pressures as well as temperatures and the details are given in [29–31]

Based on existing work [32–38], the basic proof-of-principle for both W_f/W materials (PM and CVD W_f/W) was given. The typical structure of the composite is based on wires, coated with an oxide ceramic e.g. Y_2O_3 and a W-matrix. The interface is the main vehicle to enable pseudo-ductile behaviour. W_f/W shows pseudo-ductile behaviour even at room

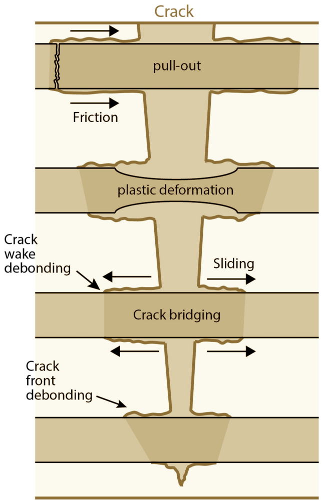

Figure 2. A selection of energy dissipation mechanisms in a fibre-composite material. Pullout of fibres, pull-out of matrix elements, crack deflection at the interface, crack bridging by fibres, crack meandering at the interface as well as plastic deformation of fibres (based on [8,35]) .

temperature for both the PM and CVD routes. This means despite crack formation, load bearing capability is retained.

When optimising the production process for W_f/W it is essential to retain as much of the properties of the constituents (e.g. wires) as possible to allow for optimal extrinsic toughening and pseudo-ductility. The interface used as well as the strength of the wire in the preform [33] are important for the overall material properties. Typically Yttria is used as interface material for the W_f/W composite due to its several advantageous properties: good thermal and chemical stability, high mechanical strength and hardness [39,40] as well as low neutron activation. To improve the CVD W_f/W material multiple avenues are being pursued including CVD parameter optimisation [29–31].

In recent times both PM and CVD processes have been scaled to allow larger sample production. In this contribution the focus lies on the CVD based W_f/W and its upscaling. In the past [35] the typically available dimensions were limited to $60 \times 60\, mm^2$. As described below the samples which are available now reach $190 \times 60\, mm^2$ and more. For the W_f/W described here no Yttria interface was applied due to the difficulty to apply it to large preforms. Work on upscaling the coating procedures for Yttria is ongoing.

3. Materials and Methods of Sample Production

The W_f/W investigated here was produced in a layer wise process (cf. fig. 3) as already described in [14,35,36]. The temperature for the process was approximately 873 K at a pressure of 100 $mbar$ and a coating time per layer of 78min. The precursor gas was heated to about 523 K to allow for a more homogenous coating of the whole preform. The volume flow of H_2 and WF_6 was 25000 $sccm$ and 2000 $sccm$ respectively.

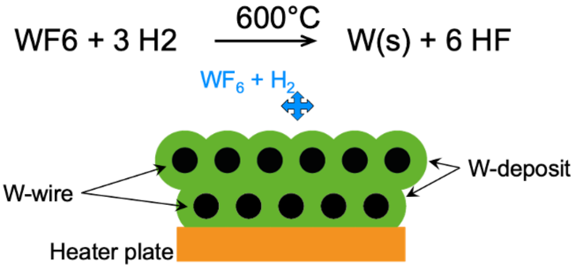

Figure 3. Process of layer-wise growth of W_f/W by applying one layer of weave at a time.

The weaves (cf fig. 4) are produced from a 150 μm potassium doped warp wire and a 50 μm potassium weft wire produced by OSRAM GmbH. For the production of dense W_f/W the optimal distance between the fibres for 150 μm is around 350 μm as described in [33]. The preforms are produced at ITA Aachen where a Mageba shuttle loom (type SL 1/80) [3] weaving machine was used to produce the weaves shown in fig. 4.

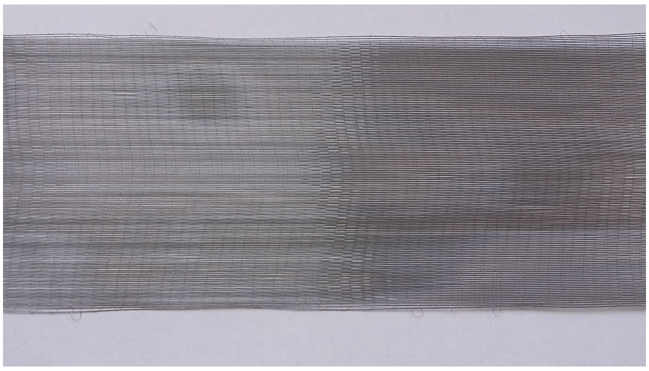

Figure 4. Tungsten weaves with 150μm wires utilised to form a 50mm wide weave.

In contrast to the samples produced and described in [14,35,36] the heating table employed had a dimension of 150x150mm employing a 5 mm thick $200 \times 200 mm^2$ tungsten plate as substrate holder. Figure 5 shows the process of placing the woven preform in two strands each $50 \times 200 mm^2$ on top of the previously coated material.

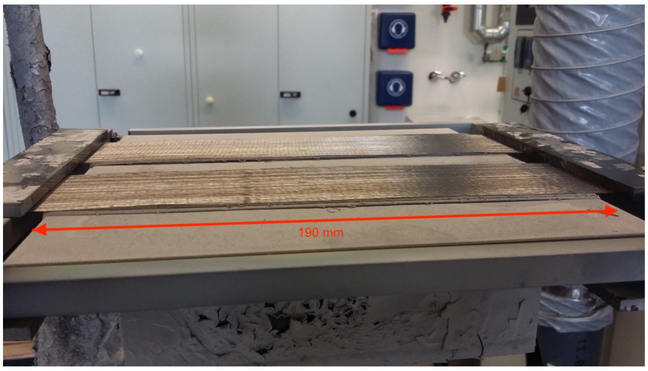

Figure 5. Heating table incl. tungsten substrate plate and Frame with weave.

In a similar manner all 23 layers of weaves are being incorporated into the composite to form finally the 10mm thick composite. During production it was already seen that one of the composite blocks showed layer delimitation after about 20 layers (cf fig 6) a typical complication of the layer-wise process.

Due to the varying layer quality care was taken to cut the samples used later from the highest quality areas. Areas with lower quality were used to cut smaller samples. From the left composite block the larger samples discussed here were produced. The right sample was used to cut KLST type samples comparable to the work in [14]. Here one difference needs to be mentioned. Where in the previous works related to CVD W_f/W the layers of the composite where always parallel to the top surface of the three point bending samples. this time they are parallel to the sides. This might not be much of a concern for an ideal material, but will have benefits as we will see later for the large samples used here.

Cutting was performed via electro discharge machining and due to delamination issues only one large and five medium sized viable sample were produced. A pre-notch was applied in the same process. In Table 1 the dimension and general properties are given.

---

[3] Mageba International GmbH, Bernkastel, Germany

doi:10.20944/preprints202210.0153.v1

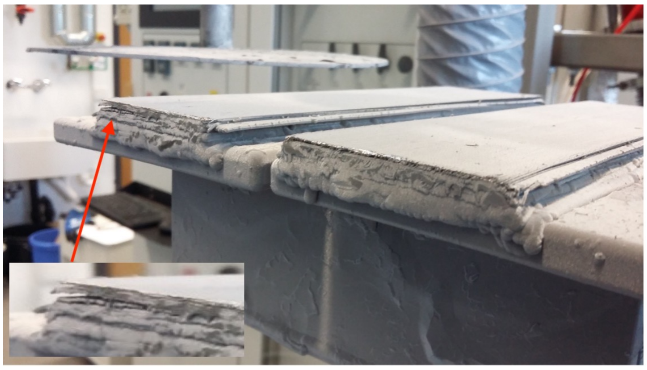

Figure 6. Side view of the samples produced after 20 layers

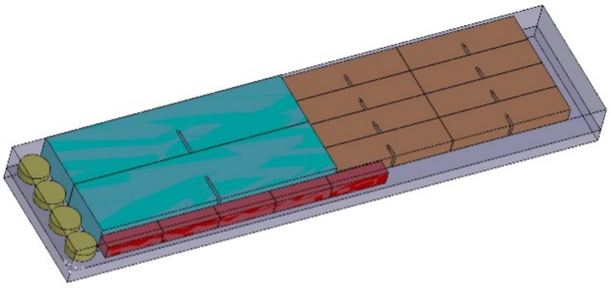

Figure 7. Cutting-plan for samples based on quality of layers

Table 1. Samples produced with their repective dimension and properties

Sample Type	Dimension (Length x Width x Height)	amount	Relative Density	Fibre-Volume-Fraction
Large	84x24x10	1	92	10.4
Medium	42x12x5	5	88-93	10.4-12.16

In comparison to [14] the samples are significantly larger while retaining similar density and fibre volume fraction.

4. Mechanical Tests

In order to compare the large scale samples in this work with the previous fracture toughness determinations [14] the 3-point bending test were performed with the same setup. A TIRAtest 2820, Nr. R050/01 from TIRA GmbH was utilised at room temperature (RT). To determine displacement and crack growth on the surface, the load-displacement curves were correlated to an optical surface observation. For the optical surface observation an optical measurement system with a tele-centric lens (OPTO ENGINEERING - TC4 M004-C) with a four times magnification was used in combination with a monochrome digital camera (Toshiba - Type DU657M). For all mechanical tests a 5 kN load cell was used. Following ASTM E399 the span for the different size samples was chosen to be 80 and 40 mm respectively. Following the ASMT 399 norm all samples were prepared with a pre-notch. Due to the use of EDM machining the Notch-tip is rounded with a 1mm EDM wire. The notch is in terms of depth is always 50% of the sample height. The notch width is 1.155mm. No additional Razor-blade or FIB sharpening was performed as from previous studies [14] and discussions with the corresponding author no need was established. The sketch for showing the sample shape is shown in 8.

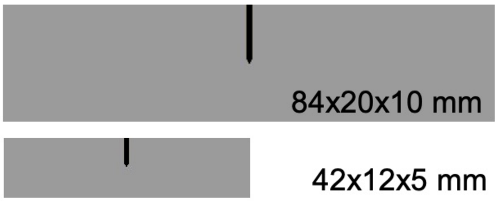

Figure 8. Sketch including pre-notch and dimensions for both the large and the medium size samples

The tests were performed with a constant displacement rate of $30\mu m/s$ for the large samples and $5\mu m/s$ for the medium samples. The camera operated at 50Hz.

5. Fracture Toughness Determination

Originally the intention was to only utilise the ASTM E399 norm, as it became apparent that also here the sample size is too small to perfectly full-fill the size requirements of ASTM E399 the data was additionally used to perform a J_Q calculation.

5.1. ASTM E399

The fracture toughness values according to ASTM E399 were calculated by analysis of load - displacement curves, with the following equation:

$$K_P = \frac{P \cdot S}{B \cdot H^{3/2}} \cdot f(a/H) \tag{1}$$

where K_P is a provisional fracture toughness, P is the load applied to the specimen, S is the span, B is the thickness, H is the height, a is the crack length and f (a/H) is a dimensionless function defined in the standard [41].

K_P is for this specimen geometry defined as K_{1C} if two size criteria are fulfilled according to [41]. The first one defines the specimen height - crack length ratio ($0.45 \leq a/H \leq 0.55$). The second size criterion defines the crack length a and the specimen thickness B. Both have to be larger than $2.5 \times (K_P/\sigma_y)^2$

For an inherently three dimensional inhomogeneous material like W_f/W the determination of the actual crack length (a) becomes complicated as the surface crack doesn't necessarily reflect on the actual crack length [42]. Despite that fact we utilised the visible crack at maximum force to get a guidance on K_P determined as $K_{R_{max}}$. The Data used for the ASTM E399 calculation is given in tab. 2

Table 2. Data for ASTM E399 calculation

Sample Type	**B [mm]**	**H [mm]**	$a_{notch}[mm]$	$a_{max}[mm]$	f(a/W)	$F_{max}[N]$	$K_{R_{max}}[MPam^{1/2}]$
Large Sample	84	10	10	8	30.83	4333.53	346.68
Medium Sample 1	42	12	5	3.5	16.69	1218.38	162.68
Medium Sample 2	42	12	5	3.5	16.69	939.03	125.38
Medium Sample 3	42	12	5	3.75	22.03	1218.93	214.78
Medium Sample 4	42	12	5	3.5	16.69	790.86	105.6
Medium Sample 5	42	12	5	3.5	16.69	806.25	107.65

5.2. ASTM 1820

As stated in [43] and re-iterated in [14] the classical application of the J-Integral is a path independent value of the stress concentration around, but excluding the crack tip. However, this holds only true with respect to path independence for straight cracks in homogenous materials with unloaded crack surfaces [44]. Despite that one can calculate a global J-Integral also applicable for composites [45] by accounting for the global amount of energy absorbed by the specimen. Here the loading of the crack surface has to be taken into account, too. This is due to the fact, that the energy absorbed within a composite material is not only in the crack tip but also behind the matrix crack tip, where extrinsic toughening is at play, such as delamination, pull-out, fibre-deformation and fibre-fracture.

The J_Q values, given in this manuscripts, are based on ASTM E1820 and [14], with the caveat that the specimens were not cyclically loaded and unloaded, to calculate J_Q, but the already utilised data of the above described 3-point bending tests was employed. This gives a guidance on the values for the two applied norms.

The J-Integral is calculated as an elastic J_{el} and a plastic J_{pl} part, as follows [46]:

$$J_{(i)} = J_{el(i)} + J_{pl(i)} \tag{2}$$

$$J_{el(i)} = \frac{(K_{(i)})^2 \cdot (1-\nu^2)}{E} \tag{3}$$

$$J_{pl(i)} = [J_{pl(i-1)} + \frac{\eta_{pl(i-1)}}{b_{(i-1)}} \cdot \frac{A_{pl(i)} - A_{pl(i-1)}}{B}] \times [1 - \gamma_{pl(i-1)} \cdot \frac{a_{(i)} - a_{(i-1)}}{b_{(i-1)}}] \tag{4}$$

Following work in [14] as well as [46] one can calculate a stress intensity factor utilising $J_{(i)}$ in the following names J_Q

$$K_Q = \sqrt{\frac{J_Q \cdot E}{1-\nu^2}} \tag{5}$$

with a valid test only given when fulfilling the size criterion $B > 10\frac{J_Q}{\sigma_y}$

K_J is calculated with the respective span given above. η_{pl} and γ_{pl} are related to crack-length and original specimen dimension where as A_{pl} is the area under the load-displacement after removing the elastic part. E is typically the Young's modulus with ν the poisson ration. i in this case gives the steps of the crack propagation utilised in the calculation instead of the cycle number. The final crack length is determined only by the surface crack length. The Young's Modulus used is $405 \cdot 10^{-3}\ Pa$ with the poisson ratio being 0.3. The Data used for the ASTM 1820 calculation is given in tab. 3

Table 3. Data for ASTM1820 calculation

Sample Type	B	H	a_{notch}	a_{max}	J_{Qmax}	$K_{Q_{max}}$
	[mm]	[mm]	[mm]	[mm]	$[Kj/m^2]$	$[MPam^{1/2}]$
Large	84	10	10	8	40.84	134.82
Medium 1	42	12	5	3.5	15.11	82.01
Medium 2	42	12	5	3.5	8.81	62.61
Medium 4	42	12	5	3.5	8.36	61.01
Medium 5	42	12	5	3.5	6.8	55.01

6. Experimental Results & Discussion

To complement the calculations given above in the following the actual force displacement curves as well as the pictures of the samples at various steps of crack-opening are given together with the J_{pl} curves.

6.1. Large sized sample

For the large sample it is quite apparent that despite dealing with a composite material the evolution of the force-displacement curve as given in fig. 9 appears very smooth indicative of the large sample size, where as the individual elements containing fibres and matrix contributed to the overall pseudo-ductile behaviour in an incremental way.

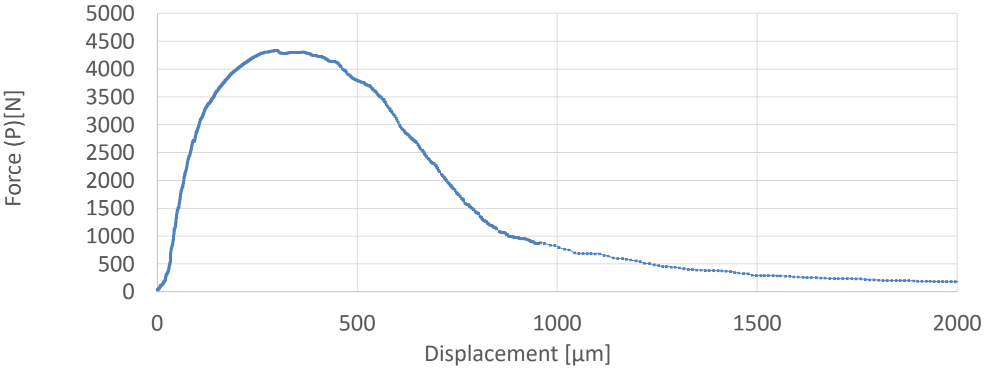

Figure 9. Force-displacement curve of large sample

Looking at the details of the fracture surfaces as given in fig. 10 one can see a few important features on the right hand side the initial notch is visible. The fracture surface is largely smooth, however to the top of the picture some of the fibre elements are not level with the rest of the fracture surface. After identifying which fibres showed necking and which didn't it can be said that 82 % of the fibres show necking which is in good agreement to the pseudo-ductile behaviour of the force-displacement curve.

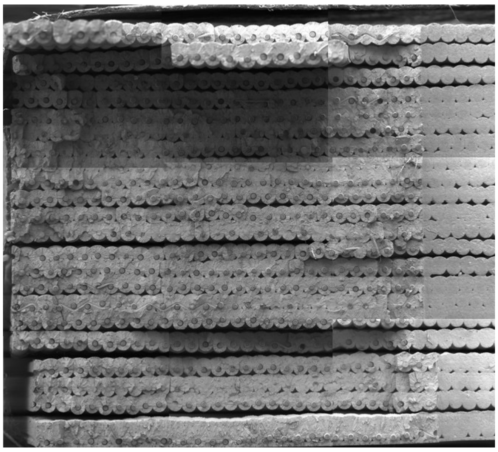

Figure 10. Composite picture of the fracture surface of the large sample with FVF and density as given in table 1

What is also visible is - that as expected - in this large sample not all layers are ideally connected. Here improvements are needed both in processing as well as textile preform manufacture to over come this. First steps to this end are studied with respect to the use of yarn-based performs as described in [47,48].

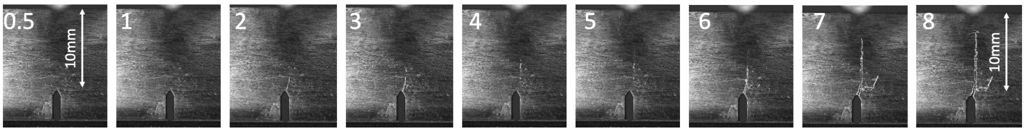

Figure 11. Crack propagation during 3-point bending test of large sample with numbers indicating the crack opening measured from the pre-notch

In contrast to previous studies such as [14] it is also visible that the individual layers are parallel to the side surfaces of the samples instead of the top.Here this mitigates the issue of interlayer delamination and improves potentially the material properties.

In figure 11 the crack opening of the large sample is shown. As already seen in the force-displacement curves the material shows stable crack growth almost all the way through the sample. The pictures shown are cropped to cover the best view of the opening crack.

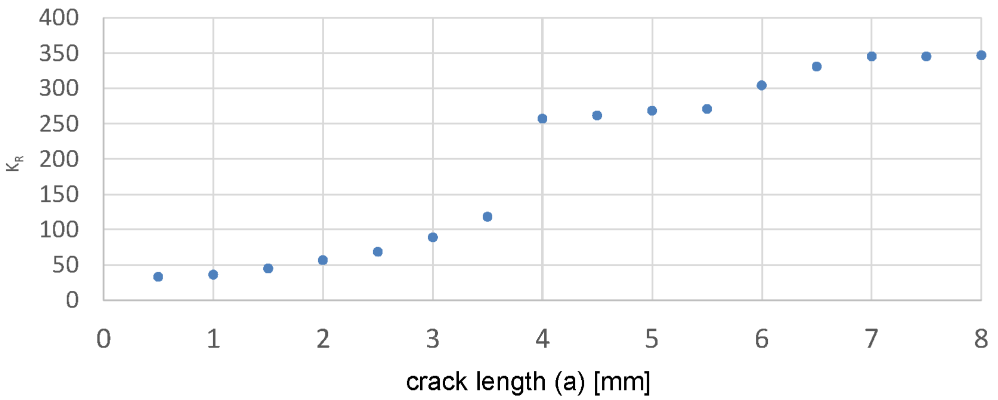

Figure 12. K_R - based on ASTM E399- values for each step of the crack opening calculated following the large samples as shown in fig. 11

Using the data obtained from figure 11 and the sample properties the plastic part of the J-Integral can be calculated as seen above the values are shown in fig. 13

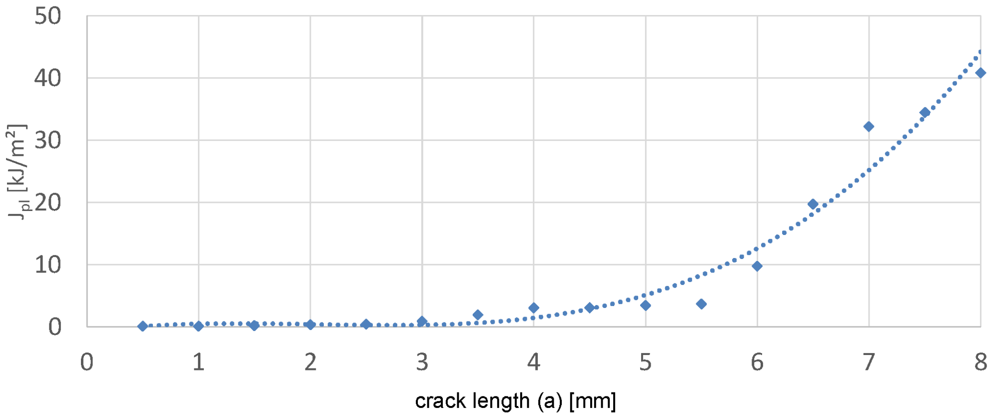

Figure 13. J_{pl} for the large sample calculated based on the sample parameters and the crack-opening shown in fig. 11

The evaluated K_R-Curves and the J_{pl}-curves for he large sample have basically a concave shape with some small plateaus. This is a mixture of the behaviour seen in [14] where no plateaus were seen and the expectations for R-Curves for homogeneous ductile materials which show a convex shape with a plateau at larger crack lengths [49].

This indicates, that here both behaviours are present. Due to the large sample size and number of unit cells (ductile fibres with matrix) resistance against crack growth is similar to homogeneous ductile materials where the resistance reaches a maximum value for a defined crack length and is overlapping with the behaviour for fibre reinforced composite where for W_f/W the extrinsic toughening mechanisms become more and more active behind the crack tip and therefore the resistance against crack growth is rising as the crack is growing. This behaviour is caused by the large scale bridging conditions and known from other fibre reinforced composites [50]. Especially the crack bridging and ductile deformation of

doi:10.20944/preprints202210.0153.v1

the fibres which become active at large crack openings are the major contribution to the toughening.

6.2. Medium sized samples

The variability of the behaviour of the medium sized samples is quite apparent. In fig 14 the different force-displacement curves show what is already known about the material. Samples 1 and 3 are fairly similar to the large sample as they are seemingly produced with relatively homogenous layer structures and thus show a very smooth trend.

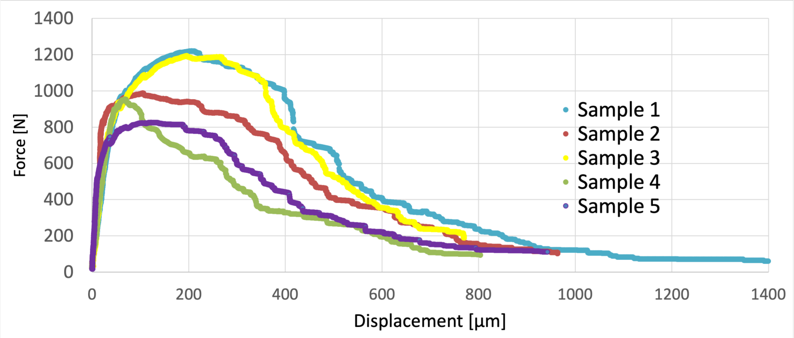

Figure 14. Force-displacement curves of medium sized samples

Due to the limited samples size one can see however larger drops in force due to the loss of fibres or fibre bundles in the composite, a typical behaviour for pseudo-ductile materials. The maximum forces of both samples are in the range of 1200N. For the the other samples either a lower maximum forces (Samples 2, 5) or a much lower load drop are visible.

This can be explained by studying the individual crack surfaces shown in figure 15.

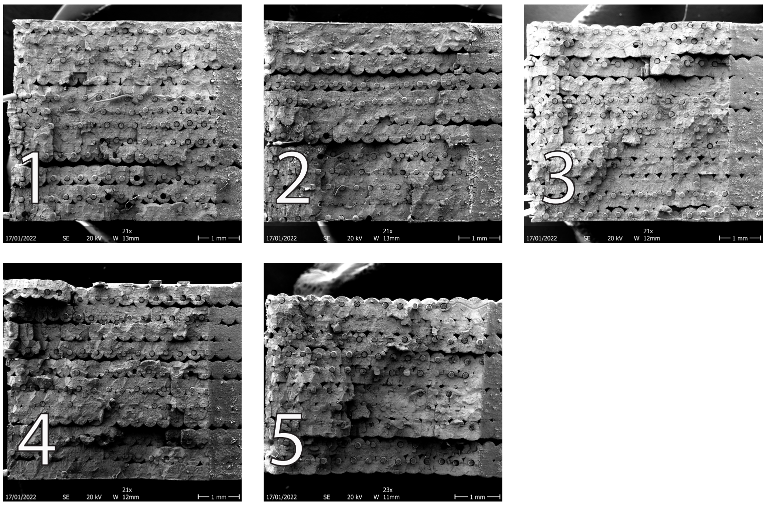

Figure 15. Pictures of the fracture surface of the individual medium sized samples

Where samples 1 and 3 show little pores and a high portion of ductile failure of the fibres leading to a height level of strength the other samples show much lower quality bonds between the layers as well as lower density. For samples 2,4,5 one can thus see that the re-distribution of force leads to local maxima and more steep drops during the 3pt bending test.

With respect to the fracture mechanical properties it also for the larger samples more or less stable crack growth is observed as shown for sample 1 in figure 16.

The opening of the crack is more difficult to follow and thus only one example is given here where the growth is most strongly visible. Based on those pictures a K value is

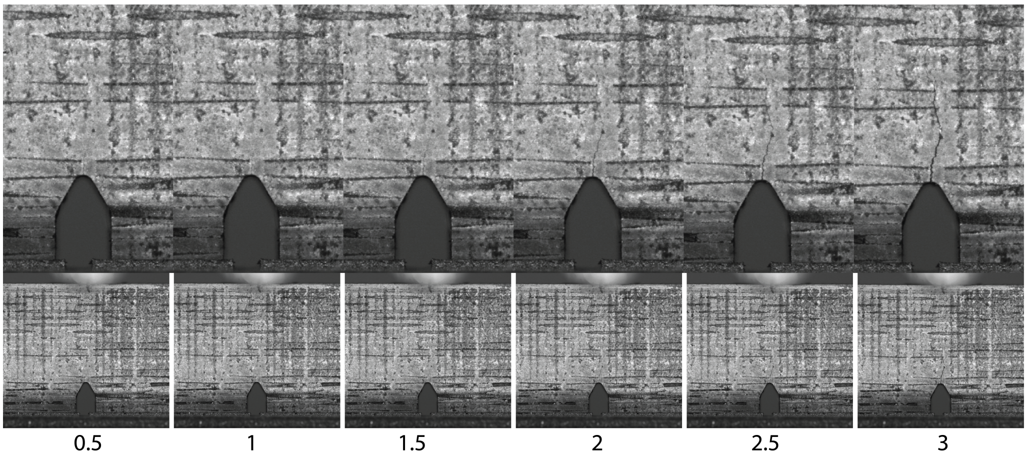

Figure 16. Crack Opening for Sample 1

calculated for the medium sized samples and plotted against the crack progress. Sample 3 is excluded as the optical data is not sufficient.

Similar to the large scale sample figure 17 displays the increase in K value with increasing crack opening.

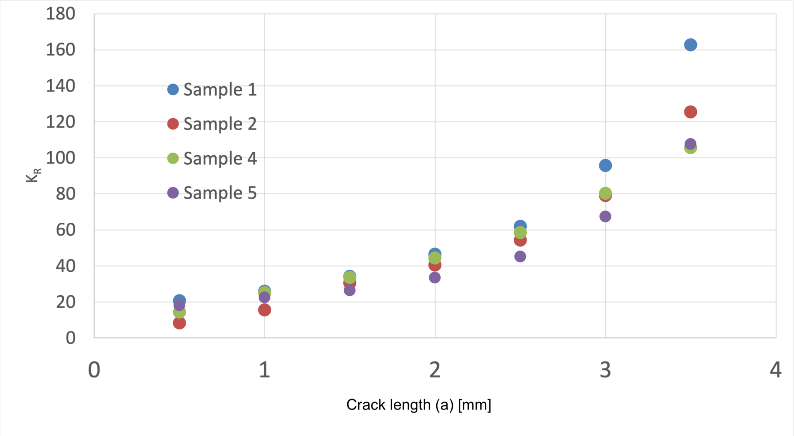

Figure 17. K_R values for each step of the crack opening calculated based on ASTM E399 following the medium sized samples. Sample 3 is missing as crack opening could not be followed.

In contrast to the large sample no plateaus are visible. it seems that thus here only the extrinsic tougnening mechanisms are the main driver for the pseudo-ductile behaviour, while for the large samples the fibres are even more important in terms of material toughening.

For the medium sized samples the K_{Rmax} values range between $105 - 162 MPam^{1/2}$

From the J_{pl} values as depicted in figure 18 a similar assessment compared to the large samples can be made. The driver for the toughening in both cases are the extrinsic mechanisms supplied by the composite in front of the crack tip.

The $J_{Q_{max}}$ values range between 6.8 and 15.11 kJ/m^2 with respective K_Q ranging between $55 - 82 MPm^{1/2}$

As a rule it seems that for W_f/W the extrinsic toughening mechanisms such as delamination, pull-out, fibre-deformation and fibre-fracture all contribute. The ductility of the fibre is one of the main mechanisms and becomes more important the larger the sample gets.

In all cases it seems that crack deflection as well as ductile deformation of fibres is a main contributor, as also shown in previous work [14].

Figure 19 shows a close up of the fracture surface of one of the medium sized samples which clearly highlights the ductile nature and contribution of the fibres.

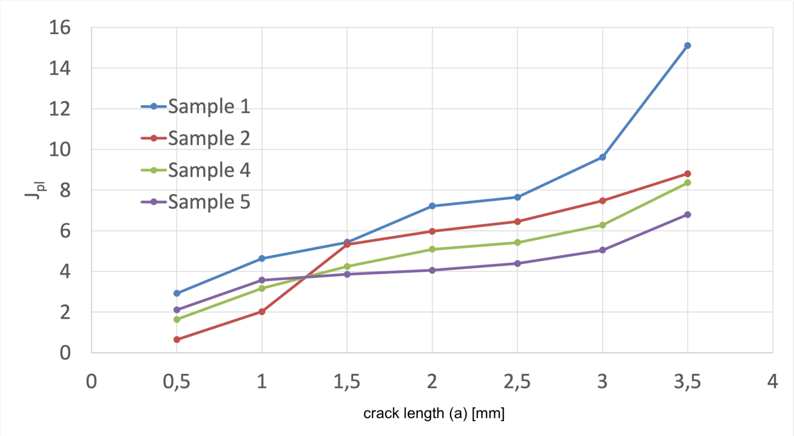

Figure 18. J_{pl} for the medium-sized samples calculated based on the sample parameters and the crack-opening similar to figure 16

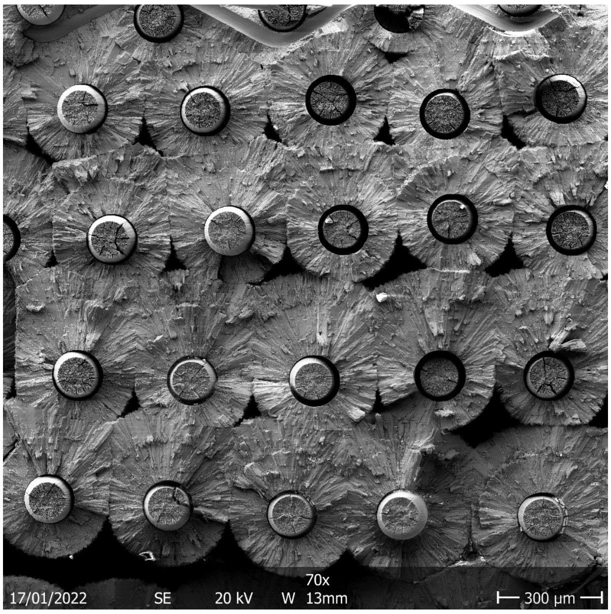

Figure 19. Fibre necking visible in the crack surface of the medium-sized sample 1

7. Summary and Conclusions

The aim of this work was to investigate the fracture behaviour and to get a first estimation for the fracture toughness of large scale long fibre W_f/W complementing the work given in [14]. According to the ASTM E399, a maximum value for the large sample of $K_{R_{max}} = 346MPam^{1/2}$ was calculated. As, the material showed a stable crack prorogation, the J-Integral approach according to ASTM E1820 was additionally applied to both sample types and a maximum value from the large sample of $J_{Q_{max}} = 41kJ/m^2(134,8MPam^{1/2})$ was determined. Even-though these samples are significantly larger as in previous studies the values given here need to the treated with care. Size criteria to fullfill the norms were not met. From the fracture surfaces it is obvious that for the materials tested here the main contribution for the pseudo-ductile behaviour originates from the fibre properties and increases the more the crack opens. This is similar to work in [14]. The composite showed stable crack propagation, crack deflection and crack stopping for all tested samples. It needs to be iterated that in case of the material studied here no interface was used. Nevertheless pseudo-ductile behaviour is observed.

From the presented study a first estimate for actual component design can be taken as the sample sizes are similar to the typical dimensions of tungsten components in ITER [51] and DEMO[52].

Acknowledgments: This work has been carried out within the framework of the EUROfusion Consortium, funded by the European Union via the Euratom Research and Training Programme (Grant Agreement No 101052200 EUROfusion). Views and opinions expressed are however those of the author(s) only and do not necessarily reflect those of the European Union or the European Commission. Neither the European Union nor the European Commission can be held responsible for them.

References

1. Pitts, R.; Carpentier, S.; Escourbiac, F.; Hirai, T.; Komarov, V.; Lisgo, S.; Kukushkin, A.; Loarte, A.; Merola, M.; Naik, A.S.; et al. A full tungsten divertor for ITER: physics issues and design status. *Journal of Nuclear Materials* **2013**, *438*, S48. https://doi.org/10.1016/j.jnucmat.2013.01.008.
2. Linsmeier, C.; Rieth, M.; Aktaa, J.; Chikada, T.; Hoffmann, A.; Hoffmann, J.; Houben, A.; Kurishita, H.; Jin, X.; Li, M.; et al. Development of advanced high heat flux and plasma-facing materials. *Nuclear Fusion* **2017**, *57*, 092007. https://doi.org/10.1088/1741-4326/aa6f71.
3. Philipps, V. Tungsten as material for plasma-facing components in fusion devices. *Journal of Nuclear Materials* **2011**, *415*, 2–9. https://doi.org/10.1016/j.jnucmat.2011.01.110.
4. Ueda, Y.; Schmid, K.; Balden, M.; Coenen J., W.; Loewenhoff, T.; Ito, A.; Hasegawa, A.; Hardie, c.; Porton, M.; Gilbert, M. Baseline high heat flux and plasma facing materials for fusion. *Nuclear Fusion* **2017**, *57*, 092006. https://doi.org/https://doi.org/10.1088/1741-4326/aa6b60.
5. You, J.; Visca, E.; Barrett, T.; Böswirth, B.; Crescenzi, F.; Domptail, F.; Fursdon, M.; Gallay, F.; Ghidersa, B.E.; Greuner, H.; et al. European divertor target concepts for DEMO: Design rationales and high heat flux performance. *Nuclear Materials and Energy* **2018**, *16*, 1–11. https://doi.org/10.1016/j.nme.2018.05.012.
6. Bachmann, C. Initial DEMO Tokamak Design Configuration Studies. In Proceedings of the http://www.soft2014.eu; , 2014; Vol. 98-99, p. 1423–1426. https://doi.org/10.1016/j.fusengdes.2015.05.027.
7. Coenen, J.; Antusch, S.; Aumann, M.; Biel, W.; Du, J.; Engels, J.; Heuer, S.; Houben, A.; Hoeschen, T.; Jasper, B.; et al. Materials for DEMO and reactor applications—boundary conditions and new concepts. *Physica Scripta* **2016**, *2016*, 014002. https://doi.org/10.1088/0031-8949/2016/T167/014002.
8. Coenen, J.W. Fusion Materials Development at Forschungszentrum Juelich. *Advanced Engineering Materials* **2020**. https://doi.org/10.1002/adem.201901376.
9. Gandhi, C.; Ashby, M. Overview no. 5. *Acta Metallurgica* **1979**, *27*, 1565–1602. https://doi.org/10.1016/0001-6160(79)90042-7.
10. Lassner, E.; Schubert, W.D. *Tungsten*; Springer US, 1999. https://doi.org/10.1007/978-1-4615-4907-9.
11. Yih, W. *Tungsten:Sources, Metallurgy, Properties, and Applications*; Springer, 1979; p. 500.
12. Barabash, V.; Federici, G.; Rödig, M.; Snead, L.; Wu, C. Neutron irradiation effects on plasma facing materials. *Journal of Nuclear Materials* **2000**, *283-287*, 138–146. https://doi.org/10.1016/s0022-3115(00)00203-8.
13. Steichen, J. Tensile properties of neutron irradiated TZM and tungsten. *Journal of Nuclear Materials* **1976**, *60*, 13–19. https://doi.org/10.1016/0022-3115(76)90112-4.
14. Gietl, H.; Olbrich, S.; Riesch, J.; Holzner, G.; Höschen, T.; Coenen, J.; Neu, R. Estimation of the fracture toughness of tungsten fibre-reinforced tungsten composites. *Engineering Fracture Mechanics* **2020**, p. 107011. https://doi.org/10.1016/j.engfracmech.2020.107011.

15. Garrison, L.M.; Katoh, Y.; Snead, L.L.; Byun, T.S.; Reiser, J.; Rieth, M. Irradiation effects in tungsten-copper laminate composite. *Journal of Nuclear Materials* **2016**, *481*, 134–146. https://doi.org/10.1016/j.jnucmat.2016.09.020.
16. Reiser, J.; Rieth, M.; Moeslang, A.; Greuner, H.; Armstrong, D.; Denk, T.; Gruening, T.; Hering, W.; Hoffmann, A.; Hoffmann, J.; et al. Tungsten (W) Laminate pipes for innovative high temperature energy conversion systems. *Advanced Engineering Materials* **2014**, *17*, 491–501. https://doi.org/10.1002/adem.201400204.
17. Rieth, M.; Dudarev, S.; Gonzalez De Vicente, S.; Aktaa, J.; Ahlgren, T.; Antusch, S.; Armstrong, D.; Balden, M.; Baluc, N.; Barthe, M.F.; et al. A brief summary of the progress on the EFDA tungsten materials program. *Journal of Nuclear Materials* **2013**, *442*, 173–180. https://doi.org/10.1016/j.jnucmat.2013.03.062.
18. Fujitsuka, M.; Tsuchiya, B.; Mutoh, I.; Tanabe, T.; Shikama, T. Effect of neutron irradiation on thermal diffusivity of tungsten–rhenium alloys. *Journal of Nuclear Materials* **2000**, *283-287*, 1148–1151. https://doi.org/10.1016/s0022-3115(00)00170-7.
19. na Qiu, N.; Zhang, Y.; Zhang, C.; Tong, H.; ping Song, X. Tensile properties of tungsten-rhenium wires with nanofibrous structure. *International Journal of Minerals, Metallurgy, and Materials* **2018**, *25*, 1055–1059. https://doi.org/10.1007/s12613-018-1656-x.
20. Antusch et al., S. Mechanical and microstructural investigations of tungsten and doped tungsten materials produced via powder injection molding. *Nuclear Materials and Energy* **2015**, *3-4*, 22–31. https://doi.org/10.1016/j.nme.2015.04.002.
21. Rieth, M.; Dudarev, S.; De Vicente, S.G.; Aktaa, J.; Ahlgren, T.; Antusch, S.; Armstrong, D.; Balden, M.; Baluc, N.; Barthe, M.F.; et al. Recent progress in research on tungsten materials for nuclear fusion applications in Europe. *Journal of Nuclear Materials* **2013**, *432*, 482–500.
22. Riesch, J.; Buffiere, J.Y.; Hoeschen, T.; di Michiel, M.; Scheel, M.; Linsmeier, C.; You, J.H. In situ synchrotron tomography estimation of toughening effect by semi-ductile fibre reinforcement in a tungsten-fibre-reinforced tungsten composite system. *Acta Materialia* **2013**, *61*, 7060–7071. https://doi.org/10.1016/j.actamat.2013.07.035.
23. Riesch, J.; Hoeschen, T.; Linsmeier, C.; Wurster, S.; You, J.H. Enhanced toughness and stable crack propagation in a novel tungsten fibre-reinforced tungsten composite produced by chemical vapour infiltration. *Physica Scripta* **2014**, *2014*, 014031. https://doi.org/10.1088/0031-8949/2014/t159/014031.
24. Mao, Y.; Coenen, J.; Sistla, S.; Liu, C.; Terra, A.; Tan, X.; Riesch, J.; Hoeschen, T.; Wu, Y.; Broeckmann, C.; et al. Design of tungsten fibre-reinforced tungsten composites with porous matrix. *Materials Science and Engineering: A* **2021**, *817*, 141361. https://doi.org/10.1016/j.msea.2021.141361.
25. Mao, Y.; Coenen, J.W.; Riesch, J.; Sistla, S.; Almanstötter, J.; Terra, A.; Chen, C.; Wu, Y.; Raumann, L.; Höschen, T.; et al. Fibre Volume Fraction Influence on Randomly Distributed Short Fibre Tungsten Fibre Reinforced Tungsten Composites. *Advanced Engineering Materials* **2020**. https://doi.org/10.1002/adem.201901242.
26. Mao, Y.; Coenen, J.W.; Sistla, S.; Tan, X.; Riesch, J.; Raumann, L.; Schwalenberg, D.; Höschen, T.; Chen, C.; Wu, Y.; et al. Development of tungsten fibre-reinforced tungsten with a porous matrix. *Physica Scripta* **2020**, *T171*, 014030. https://doi.org/10.1088/1402-4896/ab482e.
27. Jasper, B.; Coenen, J.W.; Riesch, J.; Höschen, T.; Bram, M.; Linsmeier, C. Powder Metallurgical Tungsten Fibre-Reinforced Tungsten. *Materials Science Forum* **2015**, *825*, 125–133. https://doi.org/10.4028/www.scientific.net/msf.825-826.125.
28. Jasper, B.; Schoenen, S.; Du, J.; Hoeschen, T.; Koch, F.; Linsmeier, C.; Neu, R.; Riesch, J.; Terra, A.; Coenen, J. Behavior of tungsten fibre-reinforced tungsten based on single fibre push-out study. *Nuclear Materials and Energy* **2016**, *9*, 416–421. https://doi.org/10.1016/j.nme.2016.04.010.
29. Raumann, L.; Coenen, J.; Riesch, J.; Mao, Y.; Schwalenberg, D.; Wegener, T.; Gietl, H.; Höschen, T.; Linsmeier, C.; Guillon, O. Modeling and experimental validation of a Wf/W-fabrication by chemical vapor deposition and infiltration. *Nuclear Materials and Energy* **2021**, *28*, 101048. https://doi.org/10.1016/j.nme.2021.101048.
30. Raumann, L.; Coenen, J.W.; Riesch, J.; Mao, Y.; Schwalenberg, D.; Gietl, H.; Linsmeier, C.; Guillon, O. Improving the W Coating Uniformity by a COMSOL Model-Based CVD Parameter Study for Denser Wf/W Composites. *Metals* **2021**, *11*, 1089. https://doi.org/10.3390/met11071089.
31. Raumann, L.; Coenen, J.; Riesch, J.; Mao, Y.; Gietl, H.; Höschen, T.; Linsmeier, C.; Guillon, O. Modeling and validation of chemical vapor deposition of tungsten for tungsten fibre reinforced tungsten composites. *Surface and Coatings Technology* **2020**, *381*, 124745. https://doi.org/10.1016/j.surfcoat.2019.06.065.
32. Coenen, J.; Mao, Y.; Sistla, S.; Müller, A.; Pintsuk, G.; Wirtz, M.; Riesch, J.; Hoeschen, T.; Terra, A.; You, J.H.; et al. Materials development for new high heat-flux component mock-ups for DEMO. *Fusion Engineering and Design* **2019**, *146*, 1431–1436. https://doi.org/10.1016/j.fusengdes.2019.02.098.
33. Gietl, H.; v Müller, A.; Coenen, J.; Decius, M.; Ewert, D.; Höschen, T.; Huber, P.; Milwich, M.; Riesch, J.; Neu, R. Textile preforms for tungsten fibre-reinforced composites. *Journal of Composite Materials* **2018**, *52*, 002199831877114. https://doi.org/10.1177/0021998318771149.
34. Mao, Y.; Coenen, J.; Riesch, J.; Sistla, S.; Almanstötter, J.; Jasper, B.; Terra, A.; Höschen, T.; Gietl, H.; Linsmeier, C.; et al. Influence of the interface strength on the mechanical properties of discontinuous tungsten fibre-reinforced tungsten composites produced by field assisted sintering technology. *Composites Part A: Applied Science and Manufacturing* **2018**, *107*, 342–353. https://doi.org/10.1016/j.compositesa.2018.01.022.
35. Riesch, J.; Aumann, M.; Coenen, J.; Gietl, H.; Holzner, G.; Hoeschen, T.; Huber, P.; Li, M.; Linsmeier, C.; Neu, R. Chemically deposited tungsten fibre-reinforced tungsten – The way to a mock-up for divertor applications. *Nuclear Materials and Energy* **2016**, *9*, 75–83. https://doi.org/10.1016/j.nme.2016.03.005.

36. Riesch, J.; Han, Y.; Almanstötter, J.; Coenen, J.; Höschen, T.; Jasper, B.; Zhao, P.; Linsmeier, C.; Neu, R. Development of tungsten fibre-reinforced tungsten composites towards their use in DEMO—potassium doped tungsten wire. *Physica Scripta* **2016**, *T167*, 014006. https://doi.org/10.1088/0031-8949/t167/1/014006.
37. Gietl, H.; Riesch, J.; Coenen, J.; Höschen, T.; Linsmeier, C.; Neu, R. Tensile deformation behavior of tungsten fibre-reinforced tungsten composite specimens in as-fabricated state. *Fusion Engineering and Design* **2017**, *124*, 396–400. https://doi.org/10.1016/j.fusengdes.2017.02.054.
38. Mao, Y.; Coenen, J.W.; Riesch, J.; Sistla, S.; Almanstötter, J.; Jasper, B.; Terra, A.; Höschen, T.; Gietl, H.; Bram, M.; et al. Development and characterization of powder metallurgically produced discontinuous tungsten fibre reinforced tungsten composites. *Physica Scripta* **2017**, *T170*, 014005. https://doi.org/10.1088/0031-8949/2017/t170/014005.
39. Coenen, J.; Riesch, J.; You, J.H.; Rieth, M.; Pintsuk, G.; Gietl, H.; Jasper, B.; Klein, F.; Litnovsky, A.; Mao, Y.; et al. Advanced materials for a damage resilient divertor concept for DEMO: Powder-metallurgical tungsten-fibre reinforced tungsten. *Fusion Engineering and Design* **2017**, *124*, 964–968. https://doi.org/10.1016/j.fusengdes.2016.12.006.
40. Mao, Y.; Engels, J.; Houben, A.; Rasinski, M.; Steffens, J.; Terra, A.; Linsmeier, C.; Coenen, J. The influence of annealing on yttrium oxide thin film deposited by reactive magnetron sputtering: Process and microstructure. *Nuclear Materials and Energy* **2017**, *10*, 1–8. https://doi.org/10.1016/j.nme.2016.12.031.
41. ASTM E399-90(1997) Test Method for Linear-Elastic Plane-Strain Fracture Toughness KIc of Metallic Materials. https://doi.org/10.1520/e0399-90r97.
42. Marshall, D.; Cox, B.; Evans, A. The mechanics of matrix cracking in brittle-matrix fibre composites. *Acta Metallurgica* **1985**, *33*, 2013–2021. https://doi.org/10.1016/0001-6160(85)90124-5.
43. Rice, J.R. A Path Independent Integral and the Approximate Analysis of Strain Concentration by Notches and Cracks. *Journal of Applied Mechanics* **1968**, *35*, 379–386. https://doi.org/10.1115/1.3601206.
44. Gross, D.; Seelig, T. *Bruchmechanik*; Springer, 2006; p. 327.
45. Evans, A.; Marshall, D. Overview no. 85 The mechanical behavior of ceramic matrix composites. *Acta Metallurgica* **1989**, *37*, 2567–2583. https://doi.org/10.1016/0001-6160(89)90291-5.
46. ASTM E1830-11 Test Method for Measurement of Fracture Toughness. https://doi.org/10.1520/e1820-11.
47. Coenen, J.W.; Huber, P.; Lau, A.; Raumann, L.; Schwalenberg, D.; Mao, Y.; Riesch, J.; Terra, A.; Linsmeier, C.; Neu, R. Tungsten fibre reinforced tungsten (Wf/W) using yarn based textile preforms. *Physica Scripta* **2021**, *96*, 124063. https://doi.org/10.1088/1402-4896/ac37cf.
48. Coenen, J.W.; Treitz, M.; Gietl, H.; Huber, P.; Hoeschen, T.; Raumann, L.; Schwalenberg, D.; Mao, Y.; Riesch, J.; Terra, A.; et al. The use of tungsten yarns in the production for W f /W. *Physica Scripta* **2020**, *T171*, 014061. https://doi.org/10.1088/1402-4896/ab6096.
49. Anderson, T. *Fracture Mechanics*; CRC Press, 2017. https://doi.org/10.1201/9781315370293.
50. Bloyer, D.R.; Ritchie, R.O.; Rao, K.T.V. Fracture toughness and R-Curve behavior of laminated brittle-matrix composites. *Metallurgical and Materials Transactions A* **1998**, *29*, 2483–2496. https://doi.org/10.1007/s11661-998-0220-0.
51. Pitts, R.; Carpentier, S.; Escourbiac, F.; Hirai, T.; Komarov, V.; Kukushkin, A.; Lisgo, S.; Loarte, A.; Merola, M.; Mitteau, R.; et al. Physics basis and design of the ITER plasma-facing components. *Journal of Nuclear Materials* **2011**, *415*, S957–S964. https://doi.org/DOI:10.1016/j.jnucmat.2011.01.114.
52. You, J.; Mazzone, G.; Visca, E.; Greuner, H.; Fursdon, M.; Addab, Y.; Bachmann, C.; Barrett, T.; Bonavolontà, U.; Böswirth, B.; et al. Divertor of the European DEMO: Engineering and technologies for power exhaust. *Fusion Engineering and Design* **2022**, *175*, 113010. https://doi.org/10.1016/j.fusengdes.2022.113010.